Structure of the eukaryotic translation initiation factor eIF4E in complex with 4EGI-1 reveals an allosteric mechanism for dissociating eIF4G

Evangelos Papadopoulos[a], Simon Jenni[a], Eihab Kabha[a,b], Khuloud J. Takrouri[b,c], Tingfang Yi[a], Nicola Salvi[a], Rafael E. Luna[a], Evripidis Gavathiotis[d,e], Poornachandran Mahalingam[b,f], Haribabu Arthanari[a], Ricard Rodriguez-Mias[a], Revital Yefidoff-Freedman[b,c], Bertal H. Aktas[b], Michael Chorev[b], Jose A. Halperin[b], and Gerhard Wagner[a,1]

[a]Department of Biological Chemistry and Molecular Pharmacology, Harvard Medical School, Boston, MA 02115; [b]Laboratory for Translational Research, Harvard Medical School, Cambridge, MA 02139; [c]Department of Medicine, Brigham and Women's Hospital, Boston, MA 02115; [d]Department of Pediatric Oncology, Dana-Farber Cancer Institute, Boston, MA 02215; [e]Jack and Pearl Resnick Campus, Albert Einstein College of Medicine, Bronx, NY 10461; and [f]Rowland Institute, Harvard University, Cambridge, MA 02142

The interaction of the eukaryotic translation initiation factor eIF4E with the initiation factor eIF4G recruits the 40S ribosomal particle to the 5′ end of mRNAs, facilitates scanning to the AUG start codon, and is crucial for eukaryotic translation of nearly all genes. Efficient recruitment of the 40S particle is particularly important for translation of mRNAs encoding oncoproteins and growth-promoting factors, which often harbor complex 5′ UTRs and require efficient initiation. Thus, inhibiting the eIF4E/eIF4G interaction has emerged as a previously unpursued route for developing anticancer agents. Indeed, we discovered small-molecule inhibitors of this eIF4E/eIF4G interaction (4EGIs) that inhibit translation initiation both in vitro and in vivo and were used successfully in numerous cancer–biology and neurobiology studies. However, their detailed molecular mechanism of action has remained elusive. Here, we show that the eIF4E/eIF4G inhibitor 4EGI-1 acts allosterically by binding to a site on eIF4E distant from the eIF4G binding epitope. Data from NMR mapping and high-resolution crystal structures are congruent with this mechanism, where 4EGI-1 attaches to a hydrophobic pocket of eIF4E between β-sheet$_2$ (L$_{60}$-T$_{68}$) and α-helix$_1$ (E$_{69}$-N$_{77}$), causing localized conformational changes mainly in the H$_{78}$-L$_{85}$ region. It acts by unfolding a short 3$_{10}$-helix (S$_{82}$-L$_{85}$) while extending α-helix$_1$ by one turn (H$_{78}$-S$_{82}$). This unusual helix rearrangement has not been seen in any previous eIF4E structure and reveals elements of an allosteric inhibition mechanism leading to the dislocation of eIF4G from eIF4E.

allosteric inhibitor | NMR spectroscopy | inhibitor of protein–protein interaction

The translation initiation factor eIF4E is overexpressed in numerous human cancers and drives cellular transformation, tumorigenesis, and metastatic progression in preclinical and clinical experiments. These oncogenic processes are driven selectively, increasing the translation of a subset of oncogenic mRNAs that has highly structured 5′ UTRs (1, 2) or other regulatory elements (3). eIF4E also seems to play critical roles in learning and memory (4, 5). The protein–protein interaction between eIF4E and eIF4G is a decisive event in eukaryotic protein synthesis, because the interaction of eIF4E with eIF4G is critical for the formation of the trimeric eIF4F complex consisting of eIF4E, the multidomain scaffold protein eIF4G, and RNA helicase eIF4A. This eIF4F complex along with eIF3 mediate the recruitment of the 40S ribosomal particle to the 5′ cap of mRNA. Thus, targeting the eIF4E/eIF4G interaction has emerged as an opportunity for the development of previously unavailable anticancer agents (6). Indeed, small-molecule inhibitors of this interaction (4EGIs, which bind to eIF4E and prevent eIF4G recruitment) were discovered that exhibit this desired activity in vitro and in vivo (7). These agents have now been widely used in numerous cancer–biology (8–15) and neurobiology studies (16–18).

The activity of eIF4E is regulated by the eIF4E-binding proteins (4EBPs) in a phosphorylation-dependent manner (19–21), and 4EBPs act as tumor suppressors in mice (22) by competing with eIF4G for binding to eIF4E. Cocrystal structures of eIF4E with eIF4GII$_{621–634}$ or 4EBP-1$_{51–64}$ reveal that eIF4E binds to a common YxxxxLΦ consensus motif (Φ is hydrophobic, and x is any residue) (23). In an effort to mimic the function of 4EBP, the small-molecule inhibitor 4EGI-1 was previously discovered in a high-throughput fluorescence polarization screen (7). 4EGI-1 exists in two stable E and Z isomers that bind both the cap-bound and cap-free forms of eIF4E with equilibrium dissociation constants between 10 and 20 μM in direct in vitro binding experiments using fluorescence quenching, and the Z isomer exhibits slightly higher affinity than the E isomer (Fig. 1). 4EGI-1 disrupts eIF4E/eIF4G association in vitro and in vivo, reduces viability, inhibits the proliferation of a broad spectrum of cancer cells, such as breast cancer (7, 8) and multiple myeloma (7, 9, 10), and inhibits tumor growth in animal models of human cancers, such as acute myelogenic leukemia (9) and chronic lymphocytic leukemia (14). It was shown to enhance apoptosis in cancer cell lines (7, 9, 10) and exhibited limited toxicity in an adult mouse model (8). It exhibits enhanced activity against hypoxic tumors caused by HIF-1α induced up-regulation of
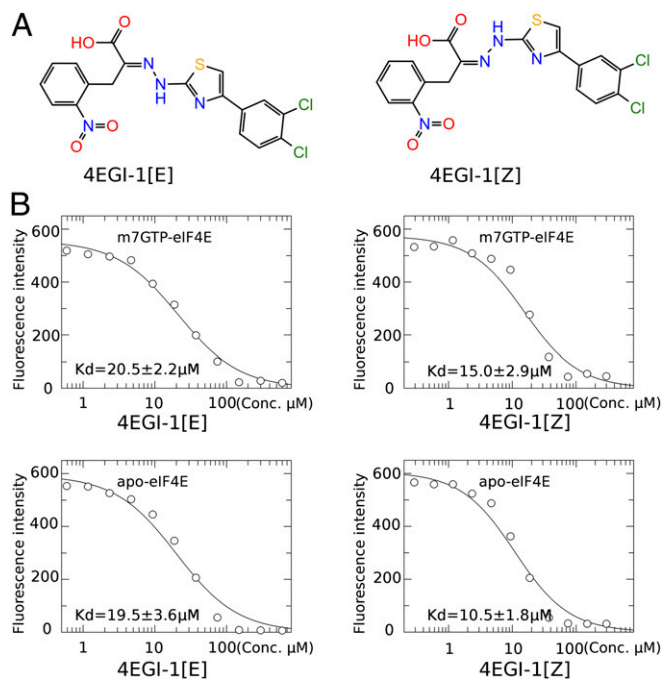
Fig. 1. 4EGI-1 chemical structure and binding affinities to cap-less (apo) and cap-bound (m^7GTP) eIF4E. (*A*) 4EGI-1 adopts two isomers with respect to the C = N double bond as indicated. Both are stable at room temperature: (*Left*) 4EGI-1[E] and (*Right*) 4EGI-1[Z]. (*B*) Binding affinities of 4EGI-1[E] or 4EGI-1[Z] to apo-GB1eIF4E or m^7GTP-GB1eIF4E as measured by intrinsic fluorescence intensity quenching. K_d values were estimated by fitting to a 1:1 stoichiometry equilibrium dissociation equation.

eIF4E (11). 4EGI-1 was also found to have antiprion activity (24) and was shown to inhibit symptoms of autism in mouse models (18, 25). However, the molecular mechanism of 4EGI-1 action, particularly its mode of binding to eIF4E and displacing eIF4G, has remained elusive. Here, we report high-resolution X-ray crystal structures of eIF4E in complexes with 4EGI-1 and two analog compounds and reveal that the inhibitors act by an allosteric mechanism.

Results

NMR Mapping of the 4EGI-1 Binding Site on eIF4E. To obtain more detailed structural insights about the mode of action of 4EGI-1, we analyzed intensity changes of signals in ^{1}H-^{13}C– and ^{1}H-^{15}N–correlated NMR spectra of eIF4E on titration with 4EGI-1[E], the more soluble isomer (Figs. S1 and S2). The data suggested an inhibitor contact site distant to the eIF4GII$_{621-634}$ peptide-binding epitope identified that was initially hypothesized as a potential binding site for 4EGI-1 (26) based on the previously determined peptide/protein cocrystal structure (23). Furthermore, 4EGI-1 did not appear to bind to a large cavity between α-helix$_1$ and α-helix$_2$, which was presumed to play a role in binding the Lassa fever virus (arenavirus) protein Z on eIF4E (27). In contrast, the NMR signals affected by 4EGI-1 binding are primarily located at a lateral surface of eIF4E between the cap-binding loop connecting strands-β$_1$ and -β$_2$ and the dorsal helices adjacent to the C-terminal end of helix-α$_1$. This 4EGI-1 binding site is distant to the eIF4G-binding site located at the N terminus of α$_1$, helix-α$_2$, and the N-terminal end of strand-β$_1$. This finding was the first indication, to our knowledge, of an allosteric mechanism of inhibition.

X-Ray Crystal Structure of the eIF4E/Inhibitor Complex. Because NMR line broadening of eIF4E spectra obtained in the presence

of 4EGI-1 did not allow the measurement of intermolecular NOEs and determination of a detailed solution NMR structure, we pursued X-ray crystallography. We succeeded to cocrystallize complexes of eIF4E with 4EGI-1[E] and two analogs (pA4EGI-1[E] and 4EGIpBr[E]), but no crystals could be grown containing Z isomers. Structures were determined by molecular replacement at 1.5–1.8 Å resolution (Fig. 2, Fig. S3, and Table S1). Ligands were unambiguously observed in unbiased difference electron density maps calculated at the early stage of structure refinement before the ligand molecules were included in the model (Fig. S3). Consistent with the NMR titrations, 4EGI-1[E] binds to an epitope distant to the eIF4GII$_{621-634}$ binding site, again suggesting an allosteric mechanism (Figs. 2 and 3 and Figs. S1 and S2). The compound stretches from a hydrophobic bay next the C terminus of helix-α$_1$ to a pocket surrounded by three basic side chains (Fig. 2*C*).

Currently, there are 27 eIF4E structures in the Protein Data Bank (PDB) database of various eIF4E constructs or homologs from human to yeast (Table S2). Our data reveal a backbone fold similar to all previous structures. Likewise, the hand-like fold of eIF4E grabs the cap nucleotide at the ventral side, whereas the dorsal helices form a dimer in the crystal with C2 pseudosymmetry (Figs. 2 and 3*A*). This dimerization contact in the crystal is similar to all structures in the PDB, except for those containing eIF4GII- or 4EBP-derived ligand peptides (23). Here, only one of the protein molecules in the pseudosymmetric dimer binds the 4EGI-1[E] analogs, indicating a 2:1 protein-to-ligand stoichiometry in the crystal. Thus, we can compare the free and ligand-bound states in the same crystal (Fig. 3 and Fig. S4).

Comparison of the Ligand-Free and the Ligand-Bound States. Differences between the ligand-bound chain A and ligand-free chain B states are plotted as rmsds on a residue level in Fig. 3*B*. Compared with the ligand-free state, the 3,4-di-chloro-phenyl moiety of 4EGI-1[E] binds to a hydrophobic groove between α$_1$-helix and β$_2$-strand and induces elongation of α$_1$-helix by one turn (H$_{78}$-L$_{85}$, Region II in Figs. 2*A* and 3*B*). This conformation change comes at the expense of a small 3$_{10}$-helix (S$_{82}$-L$_{85}$) located between helices-α$_1$ and -α$_2$ in the ligand-free eIF4E. The 3$_{10}$-helical loop disappears and migrates back in sequence to elongate helix-α$_1$ at its C terminus. The *o*-nitro-phenyl group sticks into a pocket formed by the loop between strands-β$_1$ and -β$_2$ (residues 46–64), where the backbone forms the bottom of the pocket and the side chains of K$_{49}$, K$_{54}$, and R$_{61}$ constitute the basic rim (Region I in Figs. 2*A* and 3*B*). The K$_{49}$ side chain ε-NH$_3$ forms a salt bridge with the carboxylate of 4EGI-1[E], and the R$_{61}$ side chain guanidino group engages in a cation-π interaction with the *o*-nitrophenyl group. The thiazolidine ring stacks flat onto the F$_{47}$ side chain. The entire Region I is pushed away from the dorsal helices by 4EGI-1[E]. The differences between Region III in the ligand-free and ligand-bound structures (residues K$_{119}$-D$_{125}$ in Fig. 3*B*) are located in a kink of helix-α$_2$ that connects strand-β$_4$ and may be affected by the unfolding of the adjacent 3$_{10}$-helix (S$_{82}$-L$_{85}$). The differences in Region IV (K$_{206}$-K$_{212}$) are in a less well-defined connector between helix-α$_4$ and strand-β$_8$ that contacts the triphosphate group of m^7GTP. This connector is part of one of the prongs that clamps the cap, and it also contains S$_{209}$ that can be phosphorylated by Mnk1/2 kinases (28). The C-terminal end of Region IV makes contact with 4EGI-1[E] bound in between two neighboring protein molecules in the crystal (Fig. 3). However, this protein–ligand interface is caused by crystal contacts that presumably do not exist in solution (see below).

Comparison of the eIF4E Complexes with 4EGI-1 and eIF4G. To elucidate the mechanism of allosteric inhibition, we compare the small-molecule inhibitor-bound structure and the structure in complex with eIF4GII$_{621-634}$ (Fig. 4). Fig. 4*C* reports rmsd values between structures of eIF4E bound to eIF4GII$_{621-634}$ and those
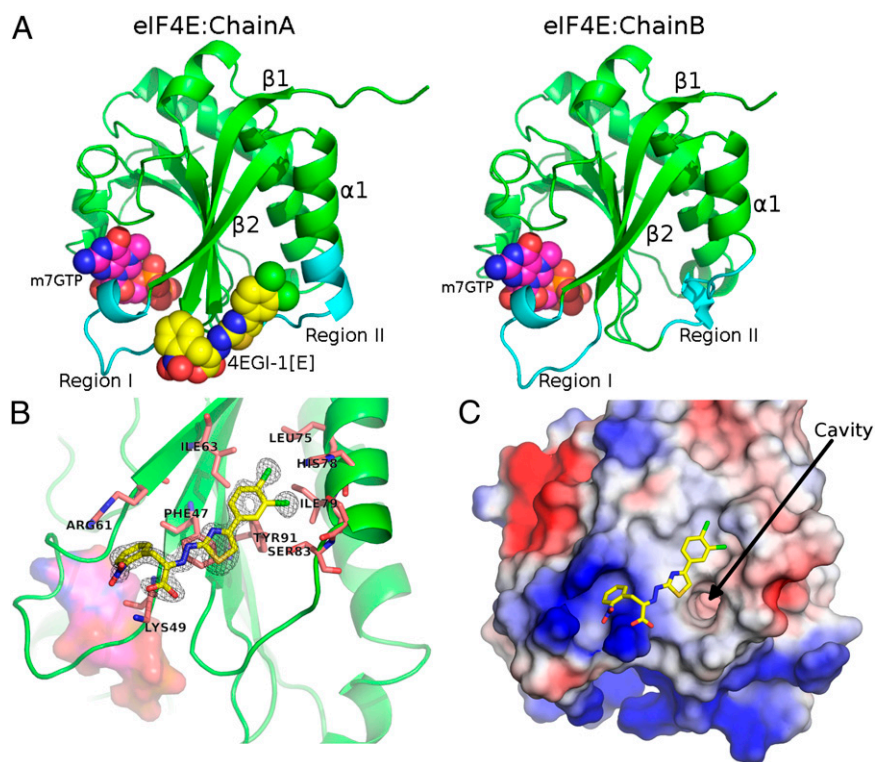
Fig. 2. Structure of eIF4E/4EGI-1[E]/m⁷GTP complex reveals binding of the inhibitor to a lateral side of eIF4E and a 2:1 protein inhibitor stoichiometry. (*A*) Side-by-side comparison between chain A (4EGI-1[E] bound) and chain B (4EGI-1[E] free) of the crystal structure. eIF4E is represented as a green cartoon, with the areas most affected and visible in cyan (Regions I and II); m⁷GTP is shown in magenta, and 4EGI-1[E] is shown with yellow carbon spheres. (*B*) Close-up view of bound compound. The green cartoon depicts eIF4E, whereas yellow sticks with mesh show 4EGI-1[E] as electron density of the unbiased F_O-F_C map before the compound was included. The magenta surface represents m⁷GTP. The key side chains of eIF4E involved in the interaction are labeled and shown as pink sticks. (*C*) Electrostatic surface representation of the 4EGI-1 binding site. The eIF4E surface is color-coded according to the electric field intensity, where blue is positive (basic) and red is negative (acidic). 4EGI-1[E] is drawn with yellow, red, and blue sticks. A cavity induced by 4EGI-1[E] binding is visible near the thiazolidine ring.

bound to either 4EGI-1[E] (Fig. 4*C*, blue bars) or ligand-free eIF4E (Fig. 4*C*, red bars). The allosteric effect seems to be related primarily to the changes in Region II, possibly Region I, and the N terminus (Fig. 4*C*, blue bars). Region III differences are just caused by the eIF4G–peptide binding or different crystal contacts. Region II is compared in detail in Fig. 4 *A* and *B*. The 4EGI-1–induced dislocation of the 3_{10}-helix (S_{82}-L_{85}) moves the side chain of Q_{80}, exposed in the eIF4E/eIF4G complex, to a position where it interacts through water molecules with D_{127} of helix-α_2, further stabilizing the new turn in helix-α_1 (Fig. 4). The side chain of H_{78}, which contacts water molecules trapped under the C-terminal residues $P_{636}A_{637}$ of the bound eIF4G peptide, moves away toward the 3,4-di-chlorophenyl moiety of bound 4EGI-1[E]. The movement of the 3_{10}-helix (S_{82}-L_{85}) from the space between helices-α_1 and -α_2 to the C terminus of α_1 opens a large cavity underneath helix-α_1 between the dorsal helices and the central β-sheet, the entrance of which is visible in Fig. 2*C* and Movies S1–S3. In the case of 4EGIpBr[E], both long and short states of helix-α_1 were observed in the electron density map, and final structure refinement resulted in a 47% occupation for the extended helix-α_1 and 53% occupation for the short helix-α_1 conformation, which indicate that this region is flexible. Helix-α_1 spans the binding sites for 4EGI-1[E] and the eIF4GII peptide and seems to be the pivotal element of the allosteric effect. The helix extension induced by 4EGI-1[E] comes with numerous additional localized structural changes. Some of them are illustrated in Fig. 4 and Movies S1–S3; Movies S1–S3 shows morphing of the transition from the eIF4G-bound state to the 4EGI-1[E]–bound conformation devoid of eIF4G.

eIF4E Oligomerization as an Inhibition Mechanism Is Not Supported by Our Data. In all three X-ray structures that we solved, the small-molecule ligand analogs of 4EGI-1 are sandwiched between two lateral protein surfaces contacting two epitopes termed Sites A and B (Figs. 3 and 5*A*). The buried solvent areas corresponding to either binding site are almost equal, which was calculated with PISA (Fig. 3*B*) (29). Each 4EGI-1 analog molecule is in a flat plane between two eIF4E molecules facing two different epitopes. Binding Site A (Fig. 3*B*, red downward facing bars) is the region between the N-terminal α-helix₁ (V_{69}-H_{78}) and the strand-β_2 (R_{61}-F_{66}), similar to the site identified with NMR mapping. This binding site, Site A, roughly corresponds to Regions I and II of the rmsd comparison between the ligand-bound chain A and the ligand-free chain B (Fig. 3*B*, blue upward facing bars). The other binding site, Site B (Fig. 3*B*, cyan downward facing bars), contacts the opposite lateral surface of the ligand 4EGI-1[E] and is formed between α-helix R_{173}-L_{187} and the C-terminal β-strand R_{214}-V_{216}. Binding Site B partially corresponds to the C-terminal Region IV of the rmsd comparison between the ligand-bound chain A and the ligand-free chain B. Compounds pA4EGI-1[E] and [E]-4EGIpBr bind in a similar way as 4EGI-1[E]. In the case of pA4EGI-1[E], the nitro-phenyl ring is rotated toward eIF4E, forming a possible hydrogen bond with the backbone (Fig. S3). Therefore, the most obvious contacts that could lead to oligomerization through the small-molecule ligands are residues belonging to Sites A and B that sandwich 4EGI-1 analogs (Fig. 5*A*).

To test whether 4EGI-1[E] binds Site A as suggested by the NMR experiments or Site B, potentially causing a compound-induced
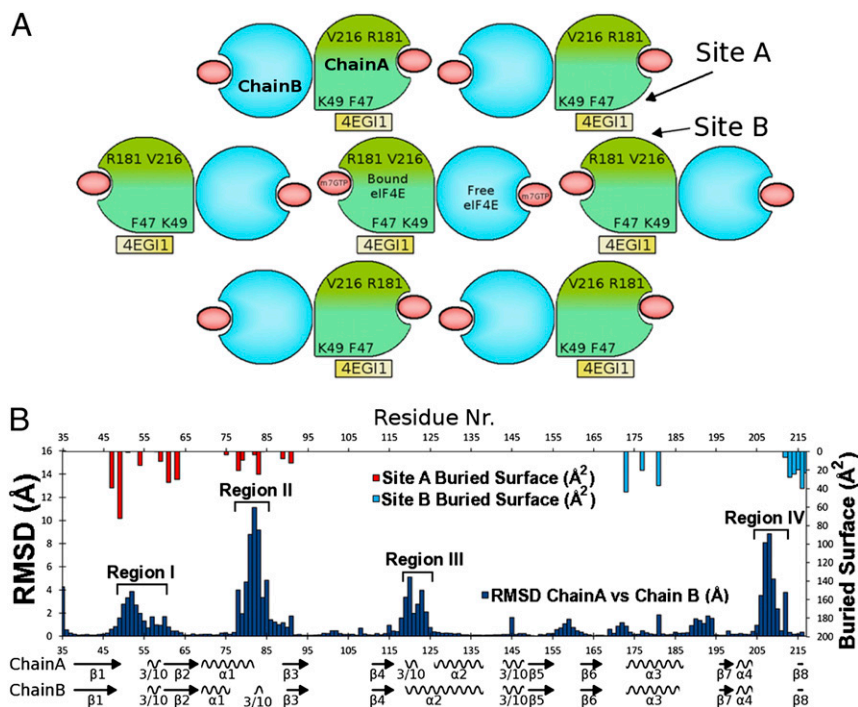
Fig. 3. eIF4E/4EGI-1[E]/m^{7}GTP complex packing and rmsd comparison of chain A to chain B shows local structural differences in four regions of eIF4E. (A) Crystal packing topology of the eIF4E/4EGI-1[E]/m^{7}GTP complex indicating positions of m^{7}GTP (red), 4EGI-1[E] (yellow), and key contact residues. The structural differences of the 4EGI-1[E]–bound chain A (green) and the 4EGI-1[E]–free chain B (blue) are symbolized with different shapes. Each eIF4E chain A contacts two 4EGI-1[E] molecules: one attached near the N terminus (Site A) and the other close to the C terminus (Site B). Thus, each 4EGI-1[E] molecule is sandwiched between two symmetrically related eIF4E chain A proteins. Binding Sites A and B are painted with different shades of green. The orientation of the proteins in the chain A and chain B columns is parallel, with the N terminus toward the bottom and the C terminus toward the top. (B) All carbon rmsds (angstroms) per residue between chain A and chain B (upward facing blue bars) compared with the surface area buried by 4EGI-1[E] (Å^2) on Sites A (downward facing red bars) and B (downward facing cyan bars). The four regions with the largest rmsd differences are indicated.

dimerization, we created the F$_{47}$A mutation, which deepens the binding pocket in Site A and the K$_{49}$A mutation, which eliminates the salt bridge between the lysine side chain and the carboxylate of the inhibitor. Indeed, the drop in the displacement curve of the fluorescence polarization (FP) assay for F$_{47}$A shifts to lower compound concentrations, signifying a stronger binding and better inhibitory activity, whereas K$_{49}$A indicates considerably weaker binding (Fig. 5B). When targeting Site B, the V$_{216}$A and R$_{181}$A mutations do not affect the compounds displacement activity (Fig. 5B), and the R$_{173}$E/T$_{177}$S/R$_{181}$A triple mutation that reverts three residues on helix-α$_3$ of Site B also does not affect the compounds displacement activity (Fig. 5D). This effect of the mutations establishes Site A as the binding site in solution, whereas compound-induced oligomerization through Sites A and B can be ruled out as the mechanism of inhibition.

However, the interface of the dorsal helices in the dimer seen in the crystal, part of which forms the peptide-binding site in the eIF4E/eIF4GII$_{621–634}$ structure (Fig. 5C), could lead to oligomerization through direct eIF4E protein–protein contacts conferred on the induced structural changes to eIF4E by 4EGI-1 analog binding. Most of the eIF4E structures in the PDB contain a dimer in the crystal with contacts through the dorsal helices (Table S2). However, there is no evidence that free eIF4E forms a dimer in solution. This monomeric state is consistent with the fact that the eIF4GII$_{621–634}$ peptide binds to this dorsal surface in the eIF4E/eIF4GII complex crystal structure. This binding event would be inhibited if the dimer would be present in solution. However, adding 4EGI-1 makes eIF4E slightly less soluble. Thus, it could be that compound binding induces oligomerization, similar to that seen in the dimer interface in crystals. Inducing this dimerization could prevent binding of eIF4G, because it uses

the same binding site. To test this hypothesis, we made several mutants targeting the contact sites observed in the crystal lattice, assuming that they would be the prime candidates for inducing aggregation in solution. We tested the mutated eIF4E for 4EGI-1[E] activity to displace the eIF4G peptide in an FP assay and displayed the IC$_{50}$ values as blue bars in Fig. 5D. Because the FP assay requires a binding-competent peptide, we also measured peptide dissociation constant K_d for all mutants as red bars in Fig. 5D. The mutants targeting the residues in the dorsal helices in the crystallographic dimer interface (Fig. 5C) are labeled C$_{(Dorsal)}$ in Fig. 5D. No IC$_{50}$ values are given for residues that disable peptide binding (L$_{135}$R and R$_{186}$E). The displacement and binding data are shown in Figs. S5 and S6. Because none of these mutants disabled 4EGI-1 inhibitory activity (no increase of IC$_{50}$), there is no evidence for inhibitor-induced dimerization through this dorsal interface.

To further test whether 4EGI-1 binding would cause oligomerization, we used measurements of ^{15}N chemical shift anisotropy/dipole–dipole (CSA/DD) cross-correlated relaxation rates to estimate the effective rotational correlation time τ$_c$ of eIF4E and its complex with 4EGI-1. Using the method by Wang et al. (30), we obtained average τ$_c$ values for the folded part of eIF4E of 15 ± 5 and 17 ± 6 ns for the free protein and the complex, respectively. Because this difference is not significant, the relaxation experiments do not support any 4EGI-1–induced oligomerization.

Of interest is L$_{131}$ in eIF4E, which makes direct contact with the conserved L$_{630}$ of eIF4G. The L$_{131}$R mutant reduced peptide affinity twofold and enhanced 4EGI-1 displacement activity threefold (Fig. 5 and Figs. S5 and S6). Located at helix-α$_2$, the residue does not make direct intermolecular contact over the
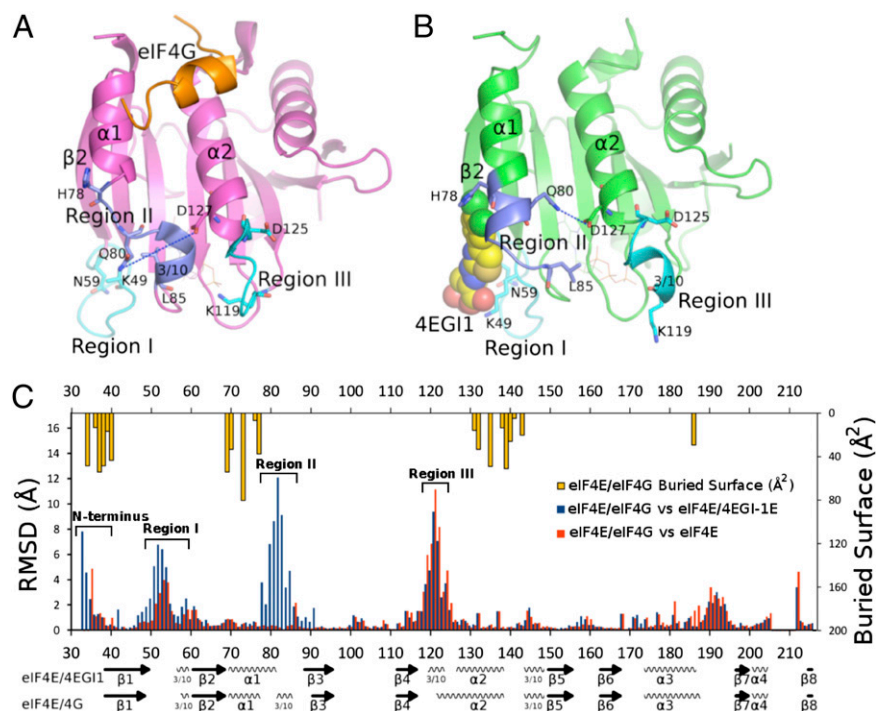
Fig. 4. The comparison between the complexes of eIF4E/4EGI-1[E] and eIF4E/eIF4GII. (*A*) Structure of the eIF4E/eIF4GII(K_{622}-A_{637}) cocomplex (PDB ID code 1EJH) is shown in the magenta cartoon. eIF4GII(K_{622}-A_{637}) is drawn in orange. The three regions with most of the differences to the eIF4E/4EGI-1[E] complex are highlighted cyan or purple. The 3_{10}-helix (S_{82}-L_{85}) is clearly seen. Q_{80} is far away from D_{127}. (*B*) Structure of the eIF4E/4EGI-1[E] cocomplex. eIF4E is green, and 4EGI-1[E] is drawn with yellow carbon spheres. The three regions with the majority of differences on the eIF4E/eIF4GII complex are highlighted cyan or purple. The 3_{10}-helix (S_{82}-L_{85}) has unfolded. An extra turn on α-helix$_1$ (H_{78}-S_{82}) has formed. Q_{80} is close to D_{127}. (*C*) All carbon rmsds (angstroms) per residue between eIF4E/eIF4GII vs. eIF4E/4EGI-1[E]:chain A (4EGI-1[E]–bound) and eIF4E/eIF4GII vs. eIF4E/4EGI-1[E]:chain B (4EGI-1[E]–free). The buried surface area (angstroms squared) per residue by eIF4GII(K_{622}-A_{637}) is indicated along the top. The regions with large differences are labeled.

noncrystallographic dimer interface but forms hydrophobic contacts with F_{72}, W_{73}, and Y_{76} of helix-α$_1$. The $L_{131}R$ mutation, thus, seems to facilitate the structural change that can also be induced by 4EGI-1[E] binding.

Extension of Helix-α$_1$ Plays a Pivotal Role in the Allosteric Displacement of eIF4G by 4EGI-1. Because small-molecule inhibitor-induced extension of helix-α$_1$ seemed to be important for the allosteric mechanism, we introduced the $N_{77}E$ and $H_{78}E$ mutations to increase helix propensity. Indeed, $N_{77}E$ exhibits an almost 10-fold lower affinity for the eIF4G peptide and twofold enhanced IC_{50} for 4EGI-1 (Fig. 5*D*), which support the notion that the helix extension and associated side-chain rearrangements are central to the allosteric mechanism. Similarly, we observe weaker peptide binding for the $H_{78}E$ mutation, which may also reflect the loss of favorable contacts to three water molecules that are simultaneously contacted by the C-terminal residues of the bound eIF4GII-derived peptide. The fact that 4EGI-1[E] is less active against this mutant is probably caused by the elimination of the histidine side chain, which interacts with the 3,4-di-chlorophenyl moiety of the inhibitor.

To further characterize the dynamic rearrangement of the protein on inhibitor binding, we initiated ^{15}N relaxation experiments. Fig. S7 displays transverse relaxation rates R2 of a B1 domain of protein G (GB1) -eIF4E fusion protein in the absence of 4EGI-1. The stability of full-length eIF4E was enhanced by the fusion with GB1 (31) and measuring at the low temperature of 10 °C. Relaxation rates could not be measured for all residues because of signal overlap, missing assignments, and broad lines at this low temperature. However, we find that helix-α$_1$ is significantly more mobile than the surrounding residues, which is indicated by the smaller rates. More comprehensive relaxation

studies and studies of the effect of 4EGI-1, eIF4G, and 4EBP-1 binding are being pursued.

Discussion

The functions of the translation initiation factor eIF4E-eIF4G complex and its assembly regulator 4EBPs are central for eukaryotic protein synthesis. The unique small-molecule 4EGI-1, which disrupts eIF4F complex and stabilizes 4EBP1 binding to eIF4E, has been an attractive tool for the understanding of translation mechanisms and a promising frame for the design of potent candidate lead compounds for cancer therapy. However, the underlying mechanisms of the inhibition have been elusive. Here, we report the crystal structure of the eIF4E/4EGI-1[E] complex at 1.5–1.8 Å resolution. The structure confirmed the location of the inhibitor-binding site indicated by NMR. Our data showed that 4EGI-1 displaces eIF4G by attaching to a hydrophobic/basic pocket of eIF4E between strand-β$_2$ (L_{60}-T_{68}) and helix-α$_1$ (E_{69}-N_{77}), elucidating the inhibitory mechanism of 4EGI-1 at atomic level. Because the compound-binding site is distant to the eIF4G-binding site, the inhibitor must act by an allosteric mechanism, and the key element seems to be helix-α$_1$, which connects the binding sites of the inhibitor and the eIF4G peptide.

Unexpectedly, in the crystal only, every other protein shows a 4EGI-1 molecule bound. Apparently, the conditions used here are not compatible with all molecules adapting identical conformations. The ligand-free copy of the protein does not show the extension of helix-α$_1$, and the site of the extension shows some electron density that may originate from molecules of the crystallization medium. It is not uncommon that proteins form asymmetric dimers in crystals, and the crystallization process captures two different states that rapidly interconvert in solution. Here, we capture two snapshots of a dynamic protein ligand
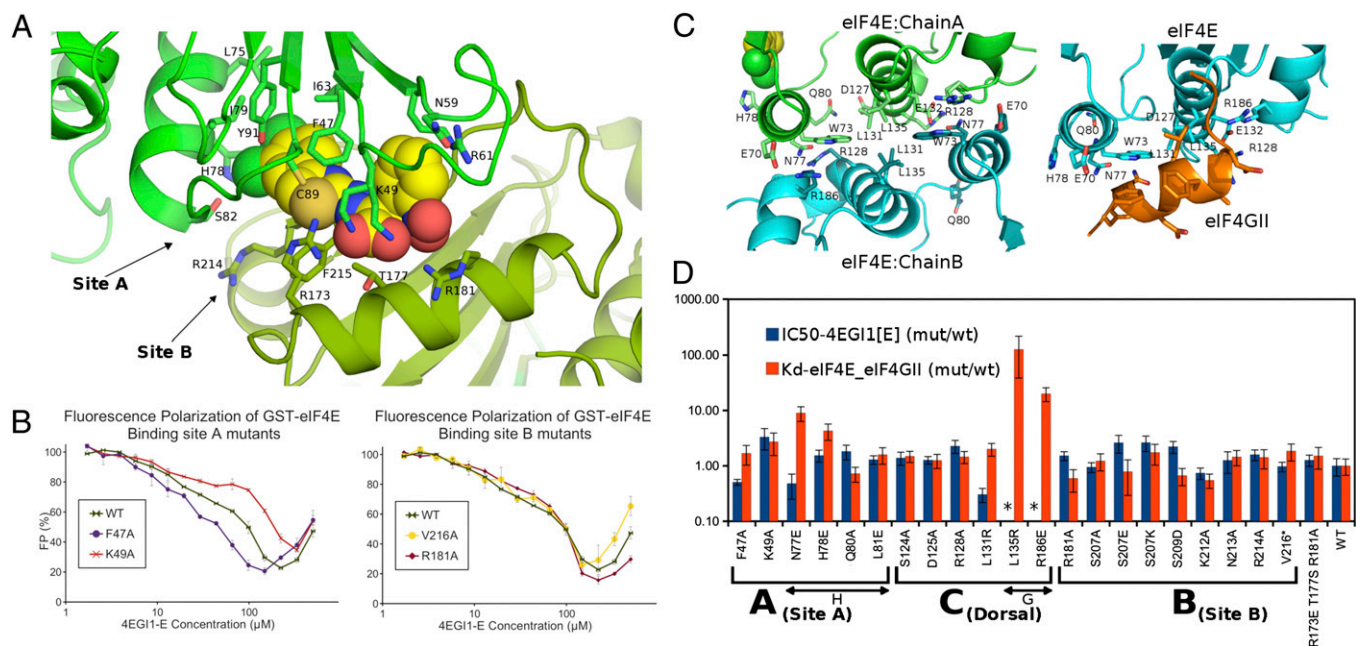
Fig. 5. Establishing the 4EGI-1 contact site in solution with site-directed mutagenesis and functional assays. (*A*) Sphere representation of 4EGI-1[E] packaged between two copies of eIF4E. The two contact sites are colored with two shades of green. Nearly all residues of Sites A and B contacting 4EGI-1[E] are labeled. Arrows point to binding Sites A and B. (*B*) FP measurements of FITC-conjugated eIF4G–peptide displacement from GST-eIF4E mutants by increasing concentrations of 4EGI-1[E]. GST-eIF4E fusions were used to enhance the difference between bound and free peptide. Disruption of the eIF4E/eIF4G–peptide complex by 4EGI-1[E] causes reduction in the FP signal. (*Left*) Mutation $F_{47}A$ increases, whereas $K_{49}A$ reduces the activity of 4EGI-1[E] on eIF4E. (*Right*) Mutations $V_{216}A$ and $R_{181}A$ do not affect the 4EGI-1[E] activity on eIF4E. A mixture of 0.5 μM mutant GST-eIF4E and 30 μM FITC-eIF4G-peptide in 100 mM Na-phosphate, pH 7.5, buffer was titrated with increasing amounts of 4EGI-1[E]. The rise of the curves beyond 120 μM is caused by loss of solubility. (*C*, *Left*) Residues in the dorsal interface between the two eIF4E molecules in the eIF4E/4EGI-1[E]/m⁷GTP complex. Chain A, shown as a green cartoon, is bound to 4EGI-1[E], whereas chain B, shown as a cyan cartoon, is not. (*C*, *Right*) Residues in the interface as defined by the eIF4E/eIF4GII complex (PDB ID code 1EJH). eIF4E is drawn in cyan, and eIF4GII(K_{622}-A_{637}) is drawn in orange. (*D*) Effect of mutations on fluorescence polarization peptide displacement activity by 4EGI-1 (IC_{50}; blue bars) and eIF4G–peptide binding (K_d; red bars). All values are normalized relative to WT eIF4E. Values were obtained by fitting the curves shown in Figs. S5 and S6. Error bars are shown, and data are plotted on a logarithmic scale. Mutants targeting Sites A and B are labeled as such. C indicates targeting the dorsal interface between eIF4E chains A and B. G indicates residues that make contact with the eIF4GII–peptide in 1EJH. They do not bind eIF4GII, which is seen by the K_d. *The IC_{50} values are meaningless.

complex. The observation that one copy does not have the inhibitor bound is consistent with the relatively weak affinity and somewhat captures two states in thermodynamic equilibrium.

To elucidate the mechanism of the allosteric effect, we used point mutations and a fluorescence polarization assay and showed that structural rearrangements, including unfolding of a short 3_{10}-helix (S_{82}-L_{85}) and elongation of helix-α_1 by one turn (H_{78}-S_{82}),

are crucial to subsequently prevent eIF4G recruitment. This model for the allosteric inhibition mechanism is supported by the observation that the helicity-enhancing mutants $N_{77}E$ and $H_{78}E$ destabilize eIF4GII peptide binding. Additional mutants to test this hypothesis are being pursued.

To further examine the role of this helix-α_1, it will be interesting to characterize the dynamics of this helix and the entire
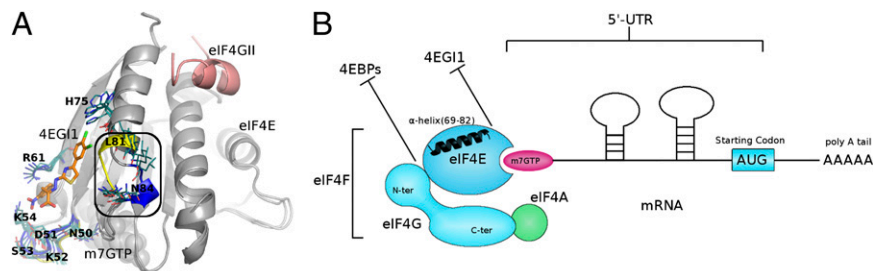

Fig. 6. The translation initiation inhibitor 4EGI-1 targets a region near the C-terminal end of α-helix$_1$(69–82) distant from the binding site of the eIF4G peptide. (*A*) Superposition of bound and free eIF4E as well as intermediate states generated by the Yale morph server is shown together with the labeled side chains of mostly affected residues. The region between L81-N84 shows a dramatic conformational change between a loop/3_{10}helix turn in the eIF4GII-bound state (blue) and an extra α-helix turn in the 4EGI-1–bound state (yellow). 4EGI-1 is shown with orange sticks, and the eIF4GII peptide is shown as a pink cartoon. The transition can be seen in Movies S1–S3. (*B*) Cartoon of the topology of the eIF4F complex (cyan) containing the cap-binding protein eIF4E (dark cyan), the scaffold protein eIF4G (light cyan), and the RNA helicase eIF4A (green). eIF4E binds the 5′ cap m⁷GTP-nucleotide (red), whereas the RNA helicase eIF4A is thought to unwind secondary structure in the 5′ UTR to clear a landing pad for the small ribosomal subunit and facilitate scanning to the start codon. The small-molecule 4EGI-1 discovered by a fluorescence polarization assay as a compound that inhibits eIF4G peptide from binding to eIF4E was presumed to bind at the same epitope. Our studies reveal that, instead, it binds to the other side of α-helix(69–82), inhibiting the eIF4G binding allosterically.

eIF4E with relaxation time measurements. Indeed, initial data indicate that helix-α_1 exhibits enhanced mobility and fluctuates between conformations. Thus, it seems that the protein adopts multiple conformational states and inhibitor binding shifts to populations that are inconsistent with binding the eIF4G peptide. All data indicate a population shift rather than an induced fit mechanism. This protein conformation change is visualized with Fig. 6A, which depicts consecutive steps of the morphing of eIF4E from the eIF4G-bound state to the 4EGI-1–bound form. A better visualization of the conformational transition can be seen in Movies S1–S3. This is not a molecular dynamics simulation of the actual pathway and kinetics of the transition but rather a linear interpolation of the two different states of the protein as captured between chain A and chain B followed by a small local energy minimization. The location of the crucial helix is indicated in the cartoon of Fig. 6B.

We anticipate that a systematic comparison of dynamic measurements of eIF4E alone and in complexes with 4EGI-1 and eIF4G will provide more detailed insights into this allosteric mechanism. However, comprehensive measurements of relaxation times are complicated by spectral overlap and will require new experimental approaches, which are being explored. Eventually, this system could become a model system for testing computational approaches for studies of allosteric effects.

Allosteric mechanisms of protein function and inhibitor action are poorly understood and represent a big challenge for advancing basic drug design. Here, we have derived a structure-based rationale for the allosteric mechanism of the disruptive function of 4EGI-1 in prying eIF4G from eIF4E by stabilizing conformational states that do not allow eIF4G binding. Furthermore, the molecular insight obtained from the structure of the eIF4E/4EGI-1[E] complex suggests a similar mechanism of action for the analogous compounds 4E1RCat and benzoic acid derivatives that were also identified by their ability to disrupt the eIF4E/eIF4G complex (26, 32). The most unexpected finding is that the 4EGI-1 binding site is located at the lateral surface of eIF4E distant to the known eIF4G fragment binding site on eIF4E. Previous studies showed that 4EGI-1 effectively disrupts full-length eIF4E–eIF4G interaction and increases 4EBP1 binding to eIF4E in cells in vivo. Structural studies of the complex between eIF4E and full-length 4EBP have not been successful because of poor solution behavior of the complex (33–35). A previously published structure of the complex between eIF4E and a short peptide from 4EBP-1 contains the conserved YxxxxLΦ motif but does not contain any of the phosphorylation sites (23). Studies of eIF4E complexes with longer 4EBP-1 fragments are being pursued together with a characterization of the consequences of truncating 4EBP-1 and the mechanisms of the stabilizing effect of 4EGI-1.

The eIF4E/4EGI-1[E] complex structure provided here may facilitate the understanding of the molecular mechanisms of eIF4F assembly and its regulation by 4EBPs, which is essential for protein synthesis control. The high-resolution structures will provide an opportunity for a structure-based optimization of the inhibitors, such as reaching the cavity shown in Fig. 2C or better using the basic site accessed here by the nitro-phenyl group. The parent compound has been shown to have antitumor activity in vitro and in vivo (8) and enhanced activity against hypoxic tumors (11). Thus, the results shown here may pave the way for the development of a panel of therapeutics that target a tumor control point at the convergence of signaling pathways relevant for tumor formation.

Materials and Methods

Protein Purification, Crystallization, and X-Ray Structural Determination.
For protein crystallization, a construct of human eIF4E with a deletion of the first 26 amino acids Δ_{26}-eIF4E was used. Transformed *Escherichia coli* (BL21) were grown in LB media, and recombinant protein expression was induced with

0.1 mM isopropyl-β-d-thiogalactopyranoside at $OD_{600} = 0.6$ overnight at 23 °C; 3 g wet cell pellet was collected per 1 L culture and kept frozen at −30 °C. The bacteria pellet from 2 L culture was resuspended in 40 mL 50 mM Tris·HCl, pH 7.5, 100 mM NaCl, 1% Triton-X, and 5 mM tris(2-carboxyethyl)phosphine (TCEP), including an EDTA free protease inhibitors tablet, lysozyme, RNase, and DNase for cell wall and nucleic acid lysis, and lysed in a cell micro-fluidizer. The lysed cells were centrifuged at 38,000 × g for 1.5 h. The supernatant was syringe-filtered and passed through a diethylaminoethylcellulose (DEAE) column equilibrated in the same buffer. The flow through was applied for 1.5 h to an adipic-agarose-m^{7}GDP column prepared as described before (36) for the purification of m^{7}GDP-binding eIF4E. The adipic-agarose-m^{7}GDP with the bound protein was washed five times with 50 mL 10 mM Hepes, pH 7.5, 125 mM NaCl, and 1 mM TCEP, and bound Δ_{26}-eIF4E was eluted four times with 10 mL buffer containing 100 μM m^{7}GTP or m^{7}GDP plus 10 mM TCEP. The eluted fractions were pooled, concentration was determined by the Bradford assay, and they were further concentrated by ultrafiltration through a 15-mL, 10-kDa-cutoff centrifuge filter to 3 mL final volume. The concentrated eluate was applied for size-exclusion chromatography to a Superdex75 16/10 preparative column (GE Healthcare) using the same buffer as in the adipic-agarose-m^{7}GDP wash step; Δ_{26}-eIF4E appeared as a single peak with an apparent molecular mass of 21 kDa. Fractions containing pure protein were pooled. TCEP was added to a final concentration of 10 mM, and the pooled fractions were concentrated to 1 mg/mL measured by light absorbance at 280 nm with a nanodrop; 1 L culture yielded about 3–5 mg pure protein.

For crystal trials, the protein was further concentrated to 9 mg/mL. Small-molecule ligand 4EGI1-[E] and analogs were dissolved in DMSO at 12.5 mM concentration based on dry powder weight. They were mixed with the concentrated protein stock at a protein:ligand stoichiometry ranging between 2:1 and 1:5, with the best results obtained in the 2:1–1:1 range. The mixtures were incubated at room temperature while the crystal trays were set up. For crystallization, the protein–compound mixture was diluted in a series of concentrations ranging from 9 to 1 mg/mL, and the sitting drop method was used with 1 μL protein–compound mixture plus 1 μL reservoir buffer containing 10–25% (vol/vol) 3.3-kDa PEG, 100 mM MES, pH 6.0, 10% (vol/vol) isopropanol, and 2 mM CaCl$_2$. Trays were kept at room temperature (20 °C) while crystals appeared and stopped growing within 2–4 d. Optimal crystal size and morphology were obtained from conditions around 7 mg/mL protein concentration and 17–20% (vol/vol) 3.3-kDa PEG.

For cryoprotection, 5% (vol/vol) glycerol was added to the crystal drop and left to equilibrate for 5 min. Crystals were mounted and flash-cooled in liquid nitrogen. Data were collected at the APS X-Ray Synchrotron Source at Argonne Laboratories, with some crystals diffracting up to 1.5 Å resolution. Reflections were indexed, integrated, and scaled using XDS (37). The crystals are monoclinic and belong to space group P2$_1$. Structures containing two eIF4E molecules per asymmetric unit were solved by molecular replacement using PDB ID code 1EJ1 as the search model in PHASER (38). Models were built in O (39) and refined with the PHENIX refinement software (40) using individual restrained coordinate and B-factor refinement combined with refinement of the parameters for TLS groups that were defined using the TLS Motion Determination server (41). Riding hydrogen atoms were included during the refinement. The final models deposited with the PDB (PDB ID codes 4TPW, 4TQB, and 4TQC) are of good quality, which was assessed using the MolProbity structure validation software (42) (Table S1).

NMR Experiments.
A protein sample for NMR was prepared using an N-terminal fusion of eIF4E with GB1-eIF4E to enhance solubility and stability (31). Transformed *E. coli* were grown in M9 minimal media supplemented with ^{13}C-ketobutyrate and ^{13}C-ketoisovalerate precursors for the selective ^{13}C labeling of isoleucine, leucine, and valine methyl residues. The protein was expressed and purified in the same way as Δ_{26}-eIF4E used for crystallization, except that the DEAE column step was omitted. Liquid-state NMR experiments were performed in a buffer containing 100 mM Na-phosphate, pH 6.5, plus 5% (vol/vol) D$_2$O used for locking and shimming. A series of ^{13}C-HSQC spectra was recorded in a 600-MHz Varian Spectrometer with the titration of different amounts of 4EGI1-[E] from a 12.5 mM stock solution in perdeuterated D$_6$-DMSO. Data were processed by NMRpipe and transferred to Sparky for spectra visualization and peak volume integration. The peak volumes were compared in a spreadsheet, and the results were transferred to PyMol for visualization and mapping on the residues and existing eIF4E protein structures.

Protein samples for ^{15}N relaxation experiments were prepared using a GB1-eIF4E construct expressed in *E. coli* grown in M9 minimal media containing D$_2$O and ^{15}NH$_4$Cl. The protein was expressed and purified as described above. The transverse relaxation constants for the narrow and

broad doublet component were measured using the method by Wang et al. (30) with a Bruker Avance III 750-MHz NMR Spectrometer equipped with a cryoprobe. The experiments were carried out at T = 5 °C. Relaxation delays of 11.1, 22.2, and 33.3 ms were used, corresponding to N/J_{NH}, in which n = 1, 2, and 3 and J_{NH} = 90 Hz. Data were processed in NMRpipe, and peak intensities were extracted using Sparky. Rotational correlation times were calculated from relaxation data using the TRACT method by Lee et al. (43) assuming a ^{15}N-^{1}H internuclear distance r_{HN} = 1.02 Å, an angle-θ between the axially symmetric ^{15}N CSA tensor, the N–H bond-θ = 17°, and a difference of the two principal components of the ^{15}N CSA tensor $\Delta\delta$ = 160 ppm.

Transverse relaxation rates R_2 were measured with the same sample on a Bruker Avance II 900-MHz Spectrometer at 10 °C using standard experiments. During the relaxation delay, the ^{15}N-transverse relaxation was refocused using a single hard 180° pulse while applying the WALTZ-16 decoupling scheme with an rf amplitude of 5 kHz to the amide protons. Relaxation delays of 12 (repeated two times), 24, 36, 48 (repeated two times), 60, 72, 84, and 96 ms were used. These values correspond to multiples of the WALTZ-16 block. Data were processed in NMRpipe, and the peak intensities, extracted using Sparky, were fitted to exponential decays in Relax. The errors on the relaxation rates were estimated by using a Monte Carlo procedure with 500 runs.

Mutations and Fluorescence Polarization Experiments. A human GSTeIF4E construct was used to study the effect of single-amino acid mutations on the 4EGI1-[E] inhibitory activity against the eIF4E/eIF4G–peptide complex formation. $F_{47}A$, $K_{49}A$, $R_{181}A$, and $V_{216}A$ mutant constructs were produced by site-directed mutagenesis. WT and mutant GST-eIF4E constructs were expressed in *E. coli* under similar conditions as the Δ_{26}-eIF4E protein described above and purified in a similar way, except without the use of DEAE column.

For fluorescence polarization, pure eIF4G-peptide conjugated with fluorescein derived by amino acid synthesis with the sequence KKQYDREFLLDFQFK-

FITCH was used. A 1-mL solution of 30 μM eIF4G-peptide plus 0.5 μM protein in 100 mM Na-phosphate, pH 7.5, buffer was prepared for each mutant and used to fill 30 μL in each well of two columns of a 384-well dark background plate, except from the first row. In the first row wells, 60 or 90 μL each GST-eIF4E-mutant/eIF4G-peptide mixture plus 4EGI1-[E] from 12.5 mM stock solution in DMSO to a final concentration of 500 μM was added. Using a multipipette, 30 or 60 μL solution was drawn from the first row and poured into the second row, henceforth creating a series of dilution by 1/2 or 2/3. The tray was read by an EnVison plate reader.

Fluorescence Quenching. Human eIF4E contains eight tryptophanes, making it a strongly fluorescent protein. This property has been exploited in previous studies (44–46). We observed that the 4EGI1[E/Z] analogs also induce quenching of the protein intrinsic fluorescence. A solution of 1 μM Apo-GB1-eIF4E that was prepared by elution with 1 M NaCl from the adipic-agarose-m^{7}GDP column or m^{7}GTP-GB1-eIF4E in 100 mM Na-phosphate, pH 7.5, buffer was prepared. On a 96-round well, flat-bottom, black-background plate, we loaded 150 μL in each well that was measured. Starting with 4EGI1(E/Z) concentrations of 300 or 150 μM, we followed with serial dilutions by a factor of two. Measurements of fluorescence intensity were obtained using top read from a FlexStation3 microplate reader. The results were fitted to a 1:1 binding equilibrium equation using the program GRAFIT 2.0, and the K_d, background fluorescence, and fluorescence intensity of 1 μM eIF4E were fitted as free parameters.

1. Pickering BM, Willis AE (2005) The implications of structured 5′ untranslated regions on translation and disease. *Semin Cell Dev Biol* 16(1):39–47.
2. Koromilas AE, Lazaris-Karatzas A, Sonenberg N (1992) mRNAs containing extensive secondary structure in their 5′ non-coding region translate efficiently in cells over-expressing initiation factor eIF-4E. *EMBO J* 11(11):4153–4158.
3. Tcherkezian J, et al. (2014) Proteomic analysis of cap-dependent translation identifies LARP1 as a key regulator of 5′TOP mRNA translation. *Genes Dev* 28(4):357–371.
4. Casadio A, et al. (1999) A transient, neuron-wide form of CREB-mediated long-term facilitation can be stabilized at specific synapses by local protein synthesis. *Cell* 99(2):221–237.
5. Sutton MA, Schuman EM (2005) Local translational control in dendrites and its role in long-term synaptic plasticity. *J Neurobiol* 64(1):116–131.
6. Silvera D, Formenti SC, Schneider RJ (2010) Translational control in cancer. *Nat Rev Cancer* 10(4):254–266.
7. Moerke NJ, et al. (2007) Small-molecule inhibition of the interaction between the translation initiation factors eIF4E and eIF4G. *Cell* 128(2):257–267.
8. Chen L, et al. (2012) Tumor suppression by small molecule inhibitors of translation initiation. *Oncotarget* 3(8):869–881.
9. Tamburini J, et al. (2009) Protein synthesis is resistant to rapamycin and constitutes a promising therapeutic target in acute myeloid leukemia. *Blood* 114(8):1618–1627.
10. Descamps G, et al. (2012) The cap-translation inhibitor 4EGI-1 induces apoptosis in multiple myeloma through Noxa induction. *Br J Cancer* 106(10):1660–1667.
11. Yi T, Papadopoulos E, Hagner PR, Wagner G (2013) Hypoxia-inducible factor-1α (HIF-1α) promotes cap-dependent translation of selective mRNAs through up-regulating initiation factor eIF4E1 in breast cancer cells under hypoxia conditions. *J Biol Chem* 288(26):18732–18742.
12. Fan S, Li Y, Yue P, Khuri FR, Sun SY (2010) The eIF4E/eIF4G interaction inhibitor 4EGI-1 augments TRAIL-mediated apoptosis through c-FLIP Down-regulation and DR5 induction independent of inhibition of cap-dependent protein translation. *Neoplasia* 12(4):346–356.
13. Hagner PR, Schneider A, Gartenhaus RB (2010) Targeting the translational machinery as a novel treatment strategy for hematologic malignancies. *Blood* 115(11):2127–2135.
14. Willimott S, Beck D, Ahearne MJ, Adams VC, Wagner SD (2013) Cap-translation inhibitor, 4EGI-1, restores sensitivity to ABT-737 apoptosis through cap-dependent and -independent mechanisms in chronic lymphocytic leukemia. *Clin Cancer Res* 19(12):3212–3223.
15. Takrouri K, et al. (2014) Structure-activity relationship study of 4EGI-1, small molecule eIF4E/eIF4G protein-protein interaction inhibitors. *Eur J Med Chem* 77:361–377.
16. Hoeffer CA, et al. (2011) Inhibition of the interactions between eukaryotic initiation factors 4E and 4G impairs long-term associative memory consolidation but not reconsolidation. *Proc Natl Acad Sci USA* 108(8):3383–3388.
17. Hoeffer CA, et al. (2013) Multiple components of eIF4F are required for protein synthesis-dependent hippocampal long-term potentiation. *J Neurophysiol* 109(1):68–76.
18. Gkogkas CG, et al. (2013) Autism-related deficits via dysregulated eIF4E-dependent translational control. *Nature* 493(7432):371–377.
19. Gingras AC, et al. (2001) Hierarchical phosphorylation of the translation inhibitor 4E-BP1. *Genes Dev* 15(21):2852–2864.
20. Pause A, et al. (1994) Insulin-dependent stimulation of protein synthesis by phosphorylation of a regulator of 5′-cap function. *Nature* 371(6500):762–767.
21. Teleman AA, Chen YW, Cohen SM (2005) 4E-BP functions as a metabolic brake used under stress conditions but not during normal growth. *Genes Dev* 19(16):1844–1848.
22. Avdulov S, et al. (2004) Activation of translation complex eIF4F is essential for the genesis and maintenance of the malignant phenotype in human mammary epithelial cells. *Cancer Cell* 5(6):553–563.
23. Marcotrigiano J, Gingras AC, Sonenberg N, Burley SK (1999) Cap-dependent translation initiation in eukaryotes is regulated by a molecular mimic of eIF4G. *Mol Cell* 3(6):707–716.
24. Allard EK, Grujic M, Fisone G, Kristensson K (2013) Prion formation correlates with activation of translation-regulating protein 4E-BP and neuronal transcription factor Elk1. *Neurobiol Dis* 58:116–122.
25. Santini E, et al. (2013) Exaggerated translation causes synaptic and behavioural aberrations associated with autism. *Nature* 493(7432):411–415.
26. Cencic R, et al. (2011) Blocking eIF4E-eIF4G interaction as a strategy to impair coronavirus replication. *J Virol* 85(13):6381–6389.
27. Volpon L, Osborne MJ, Capul AA, de la Torre JC, Borden KL (2010) Structural characterization of the Z RING-eIF4E complex reveals a distinct mode of control for eIF4E. *Proc Natl Acad Sci USA* 107(12):5441–5446.
28. Buxade M, Parra-Palau JL, Proud CG (2008) The Mnks: MAP kinase-interacting kinases (MAP kinase signal-integrating kinases). *Front Biosci* 13:5359–5373.
29. Krissinel E, Henrick K (2007) Inference of macromolecular assemblies from crystalline state. *J Mol Biol* 372(3):774–797.
30. Wang C, Rance M, Palmer AG, 3rd (2003) Mapping chemical exchange in proteins with MW > 50 kD. *J Am Chem Soc* 125(30):8968–8969.
31. Zhou P, Lugovskoy AA, Wagner G (2001) A solubility-enhancement tag (SET) for NMR studies of poorly behaving proteins. *J Biomol NMR* 20(1):11–14.
32. Cencic R, et al. (2011) Reversing chemoresistance by small molecule inhibition of the translation initiation complex eIF4F. *Proc Natl Acad Sci USA* 108(3):1046–1051.
33. Matsuo H, et al. (1997) Structure of translation factor eIF4E bound to m7GDP and interaction with 4E-binding protein. *Nat Struct Biol* 4(9):717–724.
34. Fletcher CM, et al. (1998) 4E binding proteins inhibit the translation factor eIF4E without folded structure. *Biochemistry* 37(1):9–15.
35. Gross JD, Matsuo H, Fletcher M, Sachs AB, Wagner G (2001) Interactions of the eukaryotic translation initiation factor eIF4E. *Cold Spring Harb Symp Quant Biol* 66:397–402.
36. Edery I, Altmann M, Sonenberg N (1988) High-level synthesis in Escherichia coli of functional cap-binding eukaryotic initiation factor eIF-4E and affinity purification using a simplified cap-analog resin. *Gene* 74(2):517–525.
37. Kabsch W (2010) Xds. *Acta Crystallogr D Biol Crystallogr* 66(Pt 2):125–132.
38. McCoy AJ, et al. (2007) Phaser crystallographic software. *J Appl Cryst* 40(Pt 4):658–674.

39. Jones TA, Zou JY, Cowan SW, Kjeldgaard M (1991) Improved methods for building protein models in electron density maps and the location of errors in these models. *Acta Crystallogr A* 47(Pt 2):110–119.

40. Adams PD, et al. (2010) PHENIX: A comprehensive Python-based system for macromolecular structure solution. *Acta Crystallogr D Biol Crystallogr* 66(Pt 2):213–221.

41. Painter J, Merritt EA (2006) Optimal description of a protein structure in terms of multiple groups undergoing TLS motion. *Acta Crystallogr D Biol Crystallogr* 62(Pt 4):439–450.

42. Davis IW, et al. (2007) MolProbity: All-atom contacts and structure validation for proteins and nucleic acids. *Nucleic Acids Res* 35(Web Server issue):W375–W383.

43. Lee D, Hilty C, Wider G, Wüthrich K (2006) Effective rotational correlation times of proteins from NMR relaxation interference. *J Magn Reson* 178(1):72–76.

44. McCubbin WD, Edery I, Altmann M, Sonenberg N, Kay CM (1988) Circular dichroism and fluorescence studies on protein synthesis initiation factor eIF-4E and two mutant forms from the yeast Saccharomyces cerevisiae. *J Biol Chem* 263(33):17663–17671.

45. Shen X, Tomoo K, Uchiyama S, Kobayashi Y, Ishida T (2001) Structural and thermodynamic behavior of eukaryotic initiation factor 4E in supramolecular formation with 4E-binding protein 1 and mRNA cap analogue, studied by spectroscopic methods. *Chem Pharm Bull (Tokyo)* 49(10):1299–1303.

46. Niedzwiecka A, et al. (2002) Biophysical studies of eIF4E cap-binding protein: Recognition of mRNA 5′ cap structure and synthetic fragments of eIF4G and 4E-BP1 proteins. *J Mol Biol* 319(3):615–635.